Park and Kim
Journal of Analytical Science and Technology (2024) 15:18
https://doi.org/10.1186/s40543-024-00431-7

Journal of Analytical Science and Technology

RESEARCH ARTICLE

Open Access

Electron microprobe dating of lunar zirconolite

Changkun Park[1*] and Hwayoung Kim[1]

Abstract

Zirconolite is an accessary mineral occurred in the lunar basaltic and granitic rocks and contains relatively high contents of U, Th, and Pb, which is attractive for age dating. However, very few studies have reported the crystallization ages of lunar zirconolites because of the challenge of dating lunar zirconolites due to their fine-grained size and irregular shape. In this study, we analyzed zirconolites in a granitic clast of the lunar meteorite DEW 12007 using an electron microprobe. MAN (mean atomic number) background, peak interference, and blank corrections were applied to 31 elements including U, Th, and Pb, and REEs, to obtain high-precision and high-accuracy chemical data of the zirconolites. The electron microprobe age of the zirconolites is determined to be 4332 ± 14 Ma (2σ, $n = 20$), which is consistent with the U–Pb age (4340.9 ± 7.5 Ma; 2σ) of zircon grains from the same clast measured by an ion microprobe. The precision and accuracy achieved in this study represents a notable advance compared to previously reported electron microprobe ages of lunar zirconolites. This suggests that electron microprobe dating may be applicable to extraterrestrial materials, especially for microscopic U-Th-Pb-containing minerals in the samples returned from the Moon and Mars.

Keywords Lunar zirconolite, U-Th-Pb dating, Electron microprobe, MAN background

Introduction

The ideal composition of zirconolite is $(M_I)^{2+}(M_{II})^{4+}(M_{III})^{4+}{}_2O_7$, where the M_I site is primarily occupied by Ca^{2+} and Fe^{2+}, with minor amounts of Mg^{2+}, Mn^{2+}, Zn^{2+}, Co^{2+}, Na^{+}, REE^{3+}, and Y^{3+}. The M_{II} site is mainly occupied by Zr^{4+} with minor amounts of U^{4+}, Th^{4+}, Pb^{2+}, REE^{3+}, and Y^{3+}. The M_{III} site by Ti^{4+} with minor amounts of Zr^{4+}, Fe^{3+}, Al^{3+}, Cr^{3+}, Nb^{5+}, and Ta^{5+} (Wark et al. 1973). Zirconolite is an accessary mineral found in lunar basaltic (Rasmussen et al. 2008; Wang et al. 2021; Wark et al. 1973) and granitic rocks (Seddio et al. 2013). Lunar zirconolite coexists with other accessary minerals containing Zr and/or REEs, such as baddeleyite (ZrO_2), tranquillityite ($Fe_8(Zr,Y)_2Ti_3Si_3O_{24}$), monazite ($REE(PO_4)$), apatite ($Ca_5(PO_4)_3(F,Cl,OH)$), and merrillite ($Ca_9NaMg(PO_4)_7$). The U, Th, and Pb concentrations of the zirconolites are generally lower than 0.5 wt% in the lunar mare basalt (Rasmussen et al. 2008; Wang et al. 2021; Wark et al. 1973). Zirconolite occurs as a fine-grained elongated strings in the lunar granitic rocks, and has higher concentrations of U, Th, and Pb (< ~ 2 wt%) compared to those in mare basalts (Seddio et al. 2013).

Zirconolites have generally higher U, Th, and Pb than zircon, baddeleyite, and tranquillityite in the lunar rocks. They are ideal for age dating using an ion microprobe due to their negligible amounts of common Pb (Rasmussen and Fletcher 2004; Rasmussen et al. 2008). Due to their small grain sizes, recent ion microprobe studies on lunar zirconolites have just begun to give precise ages. Zirconolites in the mare basalt 10,047 was analyzed with SHRIMP ion microprobe, giving a $^{207}Pb/^{206}Pb$ age of 3708 ± 7 Ma (2σ) (Rasmussen et al. 2008). The weighted mean $^{207}Pb/^{206}Pb$ age of 15 zirconolites with

*Correspondence:
Changkun Park
changkun@kopri.re.kr
[1] Division of Glacier & Earth Sciences, Korea Polar Research Institute, Incheon 21990, Republic of Korea

Springer Open

© The Author(s) 2024. **Open Access** This article is licensed under a Creative Commons Attribution 4.0 International License, which permits use, sharing, adaptation, distribution and reproduction in any medium or format, as long as you give appropriate credit to the original author(s) and the source, provide a link to the Creative Commons licence, and indicate if changes were made. The images or other third party material in this article are included in the article's Creative Commons licence, unless indicated otherwise in a credit line to the material. If material is not included in the article's Creative Commons licence and your intended use is not permitted by statutory regulation or exceeds the permitted use, you will need to obtain permission directly from the copyright holder. To view a copy of this licence, visit http://creativecommons.org/licenses/by/4.0/.

low U contents from lunar impact melt rock 67,955 measured by SHRIMP infers a melt-crystallization age of 4.22 ± 0.01 Ga (2σ) (Norman and Nemchin 2014). More recently, NanoSIMS was used for dating lunar zirconolite from a KREEP basalt (NWA 4485) with a beam size of ~ 1.7 μm, giving $^{207}Pb/^{206}Pb$ age of 4349 ± 5 Ma (2σ) (Wang et al. 2021).

The electron microprobe U-Th-Pb dating technique (also referred to as chemical dating or electron microprobe dating) has been widely utilized in monazite and xenotime study (Montel et al. 2018 and references therein). Electron microprobe dating has advantages over isotope dating using an ion microprobe: (1) high spatial resolution down to ~ 1 μm on minerals at 15 keV accelerating voltage, (2) non-destructive analysis to allow repetitive measurements, (3) in-situ analysis to enable a combined study of petrography, mineral chemistry, and crystallography, (4) X-ray elemental mapping to show the compositional variations, and (5) simultaneous acquisition of U-Th-Pb age and a complete chemical composition at the several tens ppm (Allaz et al. 2020). Despite the advantages above, only few studies have reported electron microprobe dating on lunar zirconolite, for example zirconolite from a granite fragment (Apollo 12,032,366-19) (Seddio et al. 2013) and a KREEP basaltic meteorite NWA 4485 (Wang et al. 2021), and the U-Th-Pb age is 3.9 ± 0.3 Ga (2σ) and 4.5 ± 0.3 Ga (2σ), respectively. However, the uncertainties of lunar zirconolite ages obtained by electron microprobe are about two orders of magnitude worse than those obtained by ion microprobe. The reported electron microprobe ages in previous studies lack meaningful accuracy due to significant uncertainties (Seddio et al. 2013; Wang et al. 2021). However, the unsuccessful application of electron microprobe dating to lunar zirconolite in the previous studies was not due to inherent limitations of the technique. Rather, it was due to insufficient use of the advantages of the electron microprobe.

Here, we present high-precision and high-accuracy U-Th-Pb ages of lunar zirconolites using an electron microprobe. We utilized state-of-the-art techniques in electron microprobe trace element analysis, including MAN (Mean Atomic Number) background (Donovan et al. 2023; Donovan and Tingle 1996) and blank correction (Donovan et al. 2011).

Sample

The Mount DeWitt 12007 (DEW 12007) is a lunar meteorite, which was found on a blue icefield in the southern Victoria Land, Antarctica, during the Korea-Italy joint expedition in the 2012–2013 season. The meteorite is a lunar regolith breccia composed of glassy impact-melt breccia, plagioclase-rich clasts, basaltic clasts, gabbroic clasts, volcanic glass beads, impact glass spherules, fine-grained symplectitic clasts, and matrix (Collareta et al. 2016; Han 2016).

A granophyric clast (designated C3) was found in a rock chip from DEW 12007, and two polished thin sections (PTS) of clast C3 were prepared for petrography, mineral chemistry, and isotopic studies (Fig. 1). Clast C3 consists of K-feldspar, silica, fayalitic olivine, and accessory phases including zircon, baddeleyite, zirconolite, tranquillityite, and apatite. Details of the petrography, mineral chemistry, and U–Pb analyses of zircon grains from a PTS (Fig. 1a) have been reported in the precious study (Han 2016). Irregular and skeletal zircon grains are observed in one PTS (Fig. 1a), while only zirconolite grains are present in the other PTS (Fig. 1b). Zirconolites occur as small grains with tranquillityite, apatite, and troilite (Fig. 1c), and as irregular strings filling the interstices of silica and K-feldspar intergrowths with lengths up to 100 μm and widths of ~ 3 μm (Fig. 1d, e). In this study, we focused on the mineral chemistry and electron microprobe ages of the zirconolite grains.

Analytical methods

Analytical setting for electron microprobe analysis of lunar zirconolite

The PTS of DEW 12007 was coated with carbon at a thickness of ~ 25 nm. The mineral chemistry of zirconolite was analyzed using a field emission electron probe microanalyzer (FE-EPMA; JEOL JXA-8530F) equipped with five wavelength dispersive X-ray spectrometers (WDS) at the Korea Polar Research Institute. Analytical setup, measurement, data processing, and matrix correction are performed using Probe for EPMA (PfE) software.

The precision of the chemical data obtained by the electron microprobe is determined by the total number of X-rays detected by the counters, and the total number of X-rays corresponds to the accelerating voltage, beam current, counting time, and counting efficiency. An accelerating voltage of 15 keV is optimal to obtain both overvoltage for K-, L-, and M-family X-rays of the REEs, U, Th, and Pb, and a suitable X-ray generating volume as small as < ~ 2–3 μm in diameter for zirconolite analysis in the sample. A Monte Carlo simulation for electron-zirconolite interaction and X-ray generating volume was performed at 15 keV using CASINO software (version 2.5.1) (Drouin et al. 2007). The simulation result shows that the X-ray volume generated from zirconolite at 15 keV is less than 2 μm with a focused beam (Additional file 1: Fig. S1).

The X-ray count rate is proportional to the beam current, so higher current promises higher precision. However, high current electron bombardment causes local heating of the sample so that high beam current can

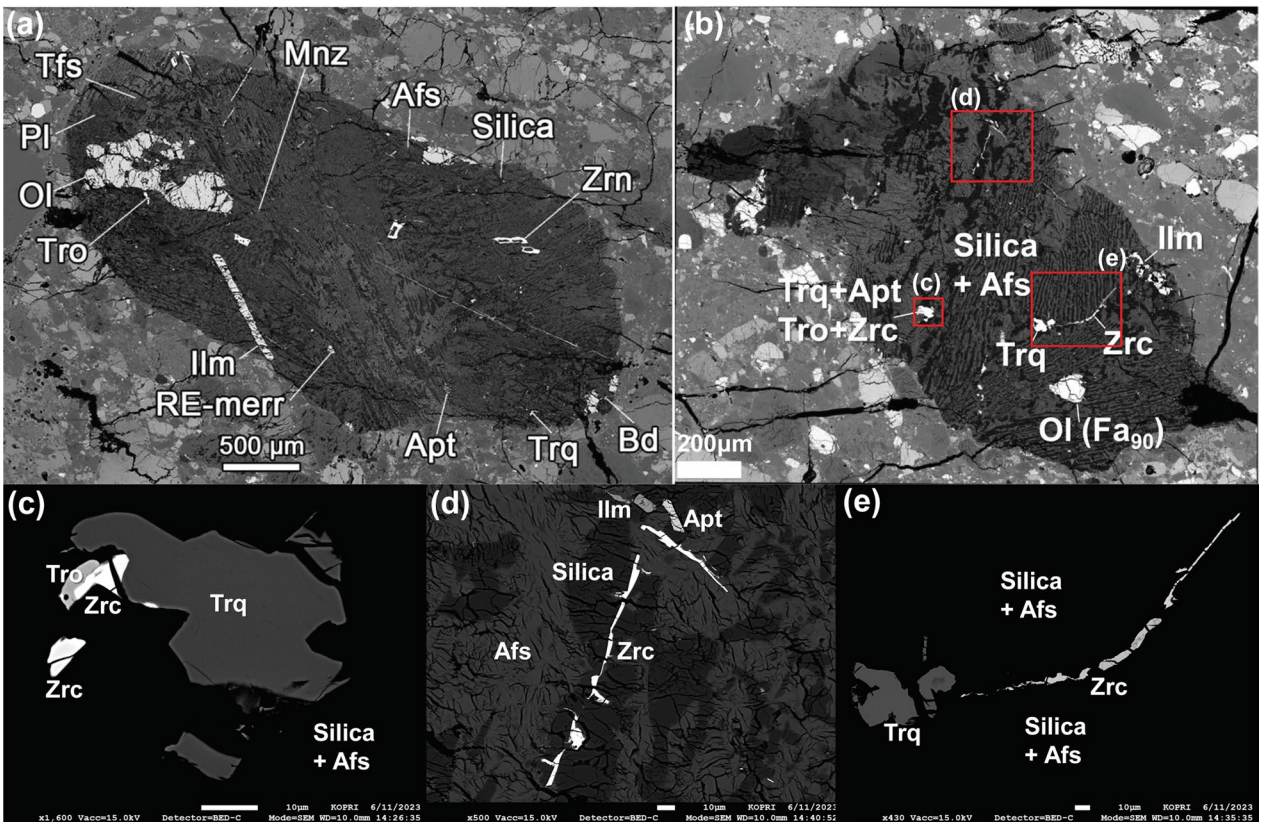

Fig. 1 A granophyric clast in the DEW 12007 (**a**) and the same clast in another PTS (**b**). The region outlined in (**b**) is shown in (**c**–**e**). Tfs: ternary feldspar, Pl: plagioclase, Ol: olivine, Tro: troilite, Ilm: ilmenite, RE-merr: REE-merrillite, Apt: apatite, Trq: tranquillityite, Bd: baddeleyite;,Zrn: zircon, Afs: Alkali feldspar, Mnz: monazite, Zrc: zirconolite

migrate mobile elements and/or damage the sample. Therefore, it is necessary to use a high beam current that does not migrate the element and does not destroy the sample. Since zirconolite is resistant to electron beam, we used 100 nA beam current in this study. At 15 keV acceleration voltage and 100 nA beam current, round pits of ~ 1.5 μm diameter were formed on the zirconolite surface with a focused beam and ~ 2 μm diameter with a 1 μm beam, respectively (Additional file 2: Fig. S2). No charging was observed due to the destruction of the carbon layer during the analysis. If there was a charging effect on the surface due to electron beam damage, this region would have appeared significantly brighter than others in the secondary electron (SE) image. However, this was not observed in Additional file 2: Fig. S2. The apparent pits in Additional file 2: Fig. S2 may be due to electron beam-induced hydrocarbon deposition obscuring the SE image (Postek 1996; Vladar and Postek 2005). Since the hydrocarbon is deposited on a thin layer of the surface less than 5 nm (Luo et al. 2010) and is as light as a carbon film, it could not significantly affect the X-ray intensities. It should also be noted that beam damage can cause element migration during the measurement, especially when a high current beam is utilized as in this study (Allaz et al. 2020). To monitor beam damage, we used a time-dependent intensity (TDI) function of the PfE software on the first element analyzed on each spectrometer. No noticeable decrease or increase in the X-ray intensities of the first elements was observed during the analyses of the lunar zirconolites. However, such contamination can increase the background intensity if the sample is coated with carbon (Allaz et al. 2020). Therefore, we adapted the MAN background correction method as described in detail below.

Lunar zirconolites have a complex elemental composition with major and numerous trace elements including REEs. If some trace elements are not measured, it will affect the overall matrix calculation. Therefore, in order to obtain accurate chemical compositions of lunar zirconolites, it is strongly recommended that all elements be measured and included in the matrix correction procedure (Moy et al. 2023). The elements to be analyzed were selected based on the literature data (Norman and Nemchin 2014; Rasmussen et al. 2008; Seddio et al. 2013; Wang et al. 2021; Wark et al. 1973). In addition, we added all REEs to obtain the REE pattern of the zirconolites

of the. Finally, a total of 31 elements were prepared for analysis (Table 1). Since REEs in lunar zirconolites are known to be generally less than ~ 1 wt%, we performed a wavescan at 15 kV, 100 nA for 0.5 s per step in monazite standard to accurately determine the peak positions of the REEs. The peak positions of Th Mα, U Mβ, and Pb Mα were determined in the zirconolite grains.

Long counting times on X-ray peaks are also required to achieve high precision, especially for minor and trace elements. In addition, long counting times for U, Th,

Table 1 Configuration of electron microprobe analysis for 31 elements in zirconolite at 15 kV and 100 nA

Element	Si Kα	Ti Kα	Al Kα	Cr Kα	Fe Kα	Mn Kα	Mg Kα	Ca Kα	Zr Lα	La Lα
Channel #	2	5	2	5	4	4	1	3	3	4
Crystal	TAP	LIFH	TAP	LIFH	LIF	LIF	TAPH	PETL	PETL	LIF
Peak (mm)	77.344	191.361	90.608	159.491	134.680	146.211	107.476	107.616	194.414	185.407
Counting time[1]	100	20	100	200	40	200	200	40	20	700
Background	MAN	MAN	MAN	MAN	MAN	MAN	MAN	MAN	MAN	MAN
Standard	Zircon	Rutile	Corundum	Eskolaite	Fayalite	Manganosite	Periclase	Wollastonite	Zircon	$LaPO_4$
Interference			Ti Kα III							
Blank (ppm)[2]										
Detection limit[3]	69	85	55	28	109	46	82	21	199	76

Element	Ce Lα	Pr Lβ	Nd Lα	Sm Lβ	Eu Lα[4]	Gd Lβ	Tb Lα	Dy Lα	Ho Lβ	Er Lα
Channel #	4	4	4	4	5	4	4	5	5	5
Crystal	LIF	LIF	LIF	LIF	LIFH	LIF	LIF	LIFH	LIFH	LIFH
Peak (mm)	178.165	157.100	164.856	139.000	147.756	128.468	137.448	133.007	114.821	124.367
Counting time	200	600	200	200	800	300	300	200	200	200
Background	MAN	MAN	MAN	MAN	MAN	MAN	MAN	MAN	MAN	MAN
Standard	$CePO_4$	$PrPO_4$	$NdPO_4$	$SmPO_4$	$EuPO_4$	$GdPO_4$	$TbPO_4$	$DyPO_4$	$HoPO_4$	$ErPO_4$
Interference					Nd Lβ3 Pr Lβ2 Mn Kα	Ho Lα		Mn Kβ		
Blank (ppm)						2.21			4.84	24.6
Detection limit	122	132	116	226	46	212	108	94	237	107

Element	Tm Lα	Y Lα	Th Mα	U Mβ	Pb Mα[4]	Yb Mα[4]	Lu Mα[4]	Hf Mα[4]	Sc Kα	Ta Mα[4]	Nb Lα
Channel #	5	3	3	3	3	2	2	2	5	2	3
Crystal	LIFH	PETL	PETL	PETL	PETL	TAP	TAP	TAP	LIFH	TAP	PETL
Peak (mm)	120.360	206.526	132.542	119.020	169.274	88.401	85.128	81.846	210.954	78.761	183.330
Counting time	600	100	400	1000	1000	200	1000	200	400	1000	200
Background	MAN	MAN	MAN	MAN	MAN	MAN	MAN	MAN	MAN	MAN	MAN
Standard	$TmPO_4$	YPO_4	Thorium Oxide	U-Glass	PbVGe-oxide	$YbPO_4$	$LuPO_4$	Hafnium metal	$ScPO_4$	Tantalum metal	Potassium Niobate
Interference				(Th M3-N4)[5] (K Kα)[5]	(Th Mζ)[5] (Y Lγ2,3)[5]	Ti Kα III Tm Mβ	Yb Mβ, Th Mβ II, U Mα II	Lu Mβ, Ti Kβ III		Hf Mβ, Y Lι	
Blank (ppm)	6.89	140	29.9	80	17.85						
Detection limit	83	106	34	35	34	333	151	204	17	189	61

[1] Counting times (s) on the X-ray peak. Background intensities were not measured but determined by the MAN method.

[2] Blank correction with the 91500 zircon standard. Data are working values from Wiedenbeck et al. (2004).

[3] Detection limits (3σ) for individual elements are reported in ppm.

[4] Measurement of Eu Lβ, Pb Mβ, Yb Lα, Lu Lα, Hf Lα, and Ta Lα is recommended for zirconolite analysis (Additional file 4: Table S3).

[5] Interference corrections for K Kα and Th on U Mβ and Th Mζ and Y Lγ2,3 on Pb Mα are estimated from Jercinovic & Williams (2005).

and Pb are essential for high-precision zirconolite dating. Counting times for each of the 31 elements were assigned based on their concentrations estimated from literature data and the wavelength scan result. Counting times at the X-ray peak position of the trace elements were set to 1000 s (Table 1). In addition, the large crystal (PETL) used for U, Th, and Pb in this study has advantages over the normal-type crystal and the H-type crystal in terms of several times higher gain, and lower noise and higher wavelength resolution, respectively (Allaz et al. 2020). This allows us to obtain very low detection limits (~ 35 ppm) on U, Th, and Pb and much higher precision on the electron microprobe ages of zirconolites compared to literature data (Seddio et al. 2013; Wang et al. 2021). It should be noted that interferences of Th Mγ on U Mβ and Th Mζ on Pb Mα may be unavoidable even when a PETL crystal is used for monazite samples because they contain ~ 5.5 to ~ 31 wt% of Th (Allaz et al. 2020). In contrast, the lunar zirconolites in this study contain ~ 1.5 wt% of ThO_2 (Table 2). Thus, the interference of Th Mγ on U Mβ and Th Mζ on Pb Mα in the zirconolite is smaller than in the monazite, but it is not negligible even in the PETL crystal (Fig. 2a, b). Moreover, the interference of Y Lγ on Pb Mα is unavoidable (Fig. 2c) and the Y_2O_3 content of the lunar zirconolites in this study is as high as ~ 6 to 8 wt% (Table 2).

Crystal type, counting time, and primary standard are listed in Table 1. A single measurement for 31 elements using 5 spectrometers took ~ 46 min. We did not measure the background intensities above and below the on-peak positions. Instead, we applied the MAN background correction described in detail in the following section.

MAN background correction

Accurate determination of the background intensity is of the most importance in trace element analysis. Several off-peak methods have been proposed and used to obtain accurate background intensities at the on-peak position of the element of interest. These include nonlinear background curve, multi-point background, and shared-background methods (Allaz et al. 2019), which are provided by the PfE software but not by the JEOL software. Despite the shared-background methods, it is very difficult to select background positions in electron microprobe analysis of zirconolite due to its complex chemistry including REEs. Numerous spectral interferences from REEs at off-peak background positions hinder accurate background correction. In particular, background intensity was observed to increase over time, possibly due to sample surface damage and contamination, especially in the carbon-coated sample with a high current beam (Allaz et al. 2020). Although zirconolite is generally resistant to electron beams, the high beam current of 100 nA used in this study for high precision may cause slight damage to the zirconolite surface, such as amorphization of the surface layer, and contamination of the carbon coating by hydrocarbon deposition. Thus MAN background correction is the solution to overcome such unexpected problem by not measuring background directly.

The MAN background correction was proposed and developed based on the fact that the background intensity is a function of the average atomic number (Donovan and Tingle 1996). Recent improvements in the MAN background correction, which using atomic fractions of the atomic numbers of the elements in the compound (Z fraction) with an exponent of ~ 0.7 (Donovan et al. 2023; Donovan and Pingitore 2002), allow us to use multi-element standards such as the Smithsonian Microanalysis Minerals to obtain accurate background intensities. To obtain accurate MAN curves for all elements measured in this study, we selected 17 standard minerals with average atomic numbers ranging from 18.7 to 35.2 (Additional file 4: Table S1). We applied the Z fraction with an exponent of 0.7 to best fit the absorption-corrected background intensities of the standard minerals. The MAN background curves for Th, U and Pb are shown in Fig. 3. Using MAN background correction, we were able to accurately determine the background intensities of 31 elements analyzed in the zirconolite and save overall measurement time by counting only the on-peak intensities of the elements. It is noteworthy that the MAN background correction method significantly improves the precision even in half the analysis time of the traditional off-peak background correction (Donovan et al. 2016).

Blank correction

Although the MAN background correction method improves precision and saves analysis time, the essential requirement for electron microprobe dating of lunar zirconolite is accuracy. In order to improve the accuracy of the MAN correction method, the "blank" correction was introduced. A secondary standard with a matrix similar to the sample (zirconolite in this study) and known concentrations of the trace elements of interest is preferred (Donovan et al. 2011, 2016). However, a zirconolite standard of known composition is not available. Instead, we tested the 91500 zircon standard for blank correction of U, Th, and Pb in the lunar zirconolite. The working values of U, Th, and Pb concentrations (80 ppm, 29.9 ppm, and 17.8 ppm, respectively) suggested by Wiedenbeck et al. (2004) were used in this study. The elements for which the blank correction was applied using the 91500 zircon standard with the blank values are listed in Table 1.

Table 2 Zirconolite compositions analyzed by electron microprobe

		#1	#2	#3	#4	#5	#6	#7	#8	#9	#10
	SiO_2	1.095	0.367	0.414	0.314	0.358	1.593	0.502	0.445	0.347	0.320
	TiO_2	29.55	30.03	30.74	30.33	30.36	30.02	30.53	30.22	30.37	30.40
	Al_2O_3	0.213	0.188	0.281	0.220	0.256	0.216	0.207	0.203	0.235	0.227
	Cr_2O_3	< 0.004	0.006	< 0.004	0.008	< 0.004	< 0.004	0.007	0.007	0.007	0.007
	FeO	7.57	7.21	6.98	7.18	7.01	7.25	7.59	7.54	7.06	7.02
	MnO	0.100	0.092	0.092	0.091	0.089	0.092	0.099	0.099	0.092	0.094
	MgO	0.317	0.129	0.208	0.117	0.163	0.046	0.084	0.095	0.188	0.078
	CaO	5.38	5.76	6.43	6.14	6.37	5.91	5.51	5.32	6.34	6.27
	ZrO2	32.06	32.32	33.67	33.64	33.60	32.91	33.12	32.54	33.42	32.88
	La_2O_3	0.155	0.423	0.282	0.296	0.276	0.151	0.161	0.142	0.315	0.311
	Ce_2O_3	1.131	2.578	1.846	1.971	1.836	1.206	1.194	1.140	1.991	1.954
	Pr_2O_3	0.231	0.449	0.327	0.363	0.351	0.236	0.269	0.247	0.368	0.351
	Nd_2O_3	1.357	1.993	1.556	1.675	1.600	1.368	1.402	1.401	1.687	1.636
	Sm_2O_3	0.670	0.634	0.543	0.566	0.532	0.564	0.665	0.686	0.546	0.543
	Eu_2O_3	< 0.005	< 0.005	< 0.005	< 0.005	< 0.005	< 0.005	< 0.005	< 0.005	< 0.005	< 0.005
	Gd_2O_3	1.194	0.979	0.874	0.906	0.885	1.014	1.169	1.220	0.875	0.890
	Tb_2O_3	0.188	0.156	0.134	0.150	0.139	0.155	0.199	0.199	0.145	0.142
	Dy_2O_3	1.344	1.062	0.940	0.995	0.985	1.141	1.381	1.429	0.956	0.967
	Ho_2O_3	0.281	0.182	0.189	0.203	0.176	0.209	0.250	0.265	0.197	0.196
	Er_2O_3	0.978	0.785	0.719	0.746	0.744	0.830	1.014	1.030	0.759	0.763
	Tm_2O_3	0.244	0.208	0.181	0.198	0.190	0.196	0.246	0.256	0.197	0.183
	Yb_2O_3	1.177	1.034	1.185	0.952	1.058	1.139	1.173	1.206	0.990	0.988
	Lu_2O_3	< 0.013	< 0.013	< 0.013	< 0.013	< 0.013	< 0.013	< 0.013	< 0.013	< 0.013	< 0.013
	Y_2O_3	7.24	6.71	6.09	6.23	6.11	6.53	7.47	7.63	6.36	6.37
	ThO_2	1.532	1.649	1.419	1.581	1.410	1.295	1.573	1.629	1.338	1.373
	UO_2	0.590	0.426	0.414	0.438	0.412	0.420	0.591	0.649	0.380	0.387
	PbO	1.037	0.862	0.760	0.853	0.757	0.767	1.039	1.131	0.727	0.747
	HfO_2	0.610	0.807	0.873	0.713	0.780	0.784	0.743	0.641	0.756	0.743
	Sc_2O_3	0.025	0.023	0.021	0.021	0.020	0.025	0.028	0.025	0.021	0.020
	Ta_2O_5	0.148	0.131	0.223	0.053	0.120	0.141	0.120	0.050	0.071	0.092
	Nb_2O_5	2.52	2.88	2.79	2.85	2.82	2.38	2.58	2.63	2.80	2.80
	Total	98.92	100.13	100.30	99.81	99.47	98.66	100.97	100.10	99.55	98.78
Cations per 7 oxygen											
A	Fe	0.4189	0.3980	0.3790	0.3939	0.3846	0.3970	0.4139	0.4160	0.3870	0.3877
	Mn	0.0056	0.0051	0.0051	0.0051	0.0050	0.0051	0.0054	0.0055	0.0051	0.0052
	Mg	0.0313	0.0127	0.0201	0.0114	0.0159	0.0044	0.0082	0.0094	0.0183	0.0076
	Ca	0.3815	0.4075	0.4477	0.4318	0.4477	0.4145	0.3852	0.3756	0.4455	0.4436
	Sum	0.8374	0.8233	0.8519	0.8422	0.8532	0.8210	0.8126	0.8065	0.8559	0.8442
B	Y	0.2550	0.2358	0.2106	0.2176	0.2132	0.2275	0.2593	0.2678	0.2220	0.2239
	Sc	0.0014	0.0013	0.0012	0.0012	0.0012	0.0014	0.0016	0.0014	0.0012	0.0012
	La	0.0038	0.0103	0.0067	0.0072	0.0067	0.0036	0.0039	0.0035	0.0076	0.0076
	Ce	0.0274	0.0623	0.0439	0.0473	0.0441	0.0289	0.0285	0.0275	0.0478	0.0473
	Pr	0.0056	0.0108	0.0077	0.0087	0.0084	0.0056	0.0064	0.0059	0.0088	0.0084
	Nd	0.0321	0.0470	0.0361	0.0392	0.0375	0.0320	0.0326	0.0330	0.0395	0.0386
	Sm	0.0153	0.0144	0.0121	0.0128	0.0120	0.0127	0.0150	0.0156	0.0123	0.0124
	Eu	–	–	–	–	–	–	–	–	–	–
	Gd	0.0262	0.0214	0.0188	0.0197	0.0192	0.0220	0.0253	0.0267	0.0190	0.0195
	Tb	0.0041	0.0034	0.0029	0.0032	0.0030	0.0033	0.0043	0.0043	0.0031	0.0031
	Dy	0.0287	0.0226	0.0197	0.0210	0.0208	0.0241	0.0290	0.0304	0.0202	0.0206

Table 2 (continued)

		#1	#2	#3	#4	#5	#6	#7	#8	#9	#10
	Ho	0.0059	0.0038	0.0039	0.0042	0.0037	0.0043	0.0052	0.0056	0.0041	0.0041
	Er	0.0203	0.0163	0.0147	0.0154	0.0153	0.0171	0.0208	0.0213	0.0156	0.0158
	Tm	0.0050	0.0043	0.0037	0.0040	0.0039	0.0040	0.0050	0.0053	0.0040	0.0038
	Yb	0.0237	0.0208	0.0235	0.0190	0.0211	0.0227	0.0233	0.0243	0.0198	0.0199
	Lu	–	–	–	–	–	–	–	–	–	–
	Sum	0.4546	0.4746	0.4055	0.4206	0.4100	0.4093	0.4601	0.4725	0.4251	0.4262
C	Zr	1.0347	1.0407	1.0665	1.0760	1.0742	1.0499	1.0533	1.0466	1.0681	1.0591
	Hf	0.0115	0.0152	0.0162	0.0134	0.0146	0.0147	0.0138	0.0121	0.0141	0.0140
	Th	0.0231	0.0248	0.0210	0.0236	0.0210	0.0193	0.0233	0.0244	0.0200	0.0206
	U	0.0087	0.0063	0.0060	0.0064	0.0060	0.0061	0.0086	0.0095	0.0055	0.0057
	Pb	0.0185	0.0153	0.0133	0.0151	0.0134	0.0135	0.0182	0.0201	0.0128	0.0133
	Sum	1.0964	1.1023	1.1229	1.1344	1.1292	1.1035	1.1173	1.1127	1.1206	1.1127
D	Si	0.0725	0.0243	0.0269	0.0206	0.0235	0.1042	0.0327	0.0293	0.0228	0.0211
	Ti	1.4707	1.4910	1.5015	1.4962	1.4971	1.4770	1.4971	1.4988	1.4970	1.5106
	Al	0.0167	0.0146	0.0215	0.0170	0.0198	0.0166	0.0159	0.0158	0.0181	0.0177
	Cr	–	0.0003	–	0.0004	–	–	0.0004	0.0004	0.0003	0.0004
	Ta	0.0027	0.0023	0.0039	0.0009	0.0021	0.0025	0.0021	0.0009	0.0013	0.0017
	Nb	0.0755	0.0859	0.0819	0.0844	0.0835	0.0705	0.0761	0.0783	0.0830	0.0835
	D	1.6380	1.6185	1.6358	1.6195	1.6260	1.6708	1.6242	1.6236	1.6225	1.6349
M_I	A	0.8374	0.8233	0.8519	0.8422	0.8532	0.8210	0.8126	0.8065	0.8559	0.8442
	B	0.1626	0.1767	0.1481	0.1578	0.1468	0.1790	0.1874	0.1935	0.1441	0.1558
	Sum	1.0000	1.0000	1.0000	1.0000	1.0000	1.0000	1.0000	1.0000	1.0000	1.0000
M_{II}	C	0.7080	0.7021	0.7426	0.7372	0.7369	0.7697	0.7272	0.7210	0.7190	0.7297
	B	0.2920	0.2979	0.2574	0.2628	0.2631	0.2303	0.2728	0.2790	0.2810	0.2703
	Sum	1.0000	1.0000	1.0000	1.0000	1.0000	1.0000	1.0000	1.0000	1.0000	1.0000
M_{III}	D	1.6380	1.6185	1.6358	1.6195	1.6260	1.6708	1.6242	1.6236	1.6225	1.6349
	Zr	0.3884	0.4002	0.3803	0.3972	0.3924	0.3338	0.3900	0.3917	0.4016	0.3831
	Sum	2.0264	2.0187	2.0161	2.0167	2.0184	2.0046	2.0143	2.0153	2.0240	2.0179
	$M_I + M_{II} + M_{III}$	4.0264	4.0187	4.0161	4.0167	4.0184	4.0046	4.0143	4.0153	4.0240	4.0179
		#11	**#12**	**#13**	**#14**	**#15**	**#16**	**#17**	**#18**	**#19**	**#20**
	SiO_2	0.364	0.380	1.361	0.579	0.638	1.411	1.183	0.806	0.338	0.800
	TiO_2	30.64	30.39	29.44	29.99	30.42	30.47	29.72	29.53	30.17	30.73
	Al_2O_3	0.228	0.252	0.196	0.197	0.360	0.659	0.341	0.259	0.200	0.380
	Cr_2O_3	0.008	0.007	0.010	0.009	0.007	0.007	0.004	< 0.004	< 0.004	0.005
	FeO	7.01	7.14	7.68	7.62	7.33	7.21	7.44	7.49	7.62	7.15
	MnO	0.092	0.092	0.101	0.103	0.094	0.102	0.100	0.097	0.100	0.089
	MgO	0.091	0.126	0.132	0.140	0.157	0.158	0.019	0.044	0.142	0.102
	CaO	6.42	6.22	4.87	5.09	5.70	5.83	5.17	5.05	5.32	6.05
	ZrO2	33.04	33.10	30.69	31.15	32.07	32.62	31.96	31.76	32.23	34.25
	La_2O_3	0.288	0.292	0.124	0.128	0.156	0.170	0.130	0.132	0.147	0.195
	Ce_2O_3	1.911	1.897	1.004	1.043	1.180	1.236	1.059	1.046	1.119	1.421
	Pr_2O_3	0.348	0.350	0.227	0.256	0.254	0.258	0.228	0.232	0.245	0.290
	Nd_2O_3	1.594	1.598	1.310	1.351	1.414	1.407	1.339	1.319	1.414	1.549
	Sm_2O_3	0.538	0.551	0.669	0.685	0.607	0.617	0.631	0.644	0.667	0.633
	Eu_2O_3	< 0.005	< 0.005	< 0.005	< 0.005	< 0.005	< 0.005	< 0.005	< 0.005	< 0.005	< 0.005
	Gd_2O_3	0.833	0.833	1.282	1.240	1.143	1.114	1.233	1.216	1.178	1.052
	Tb_2O_3	0.139	0.150	0.230	0.219	0.201	0.177	0.199	0.210	0.202	0.174
	Dy_2O_3	0.914	0.942	1.635	1.559	1.353	1.316	1.478	1.496	1.409	1.151
	Ho_2O_3	0.179	0.217	0.359	0.314	0.269	0.249	0.284	0.292	0.290	0.208

Table 2 (continued)

		#11	#12	#13	#14	#15	#16	#17	#18	#19	#20
	Er_2O_3	0.725	0.752	1.173	1.133	0.990	0.951	1.046	1.061	1.014	0.794
	Tm_2O_3	0.190	0.201	0.285	0.267	0.235	0.228	0.237	0.240	0.248	0.198
	Yb_2O_3	1.009	1.034	1.340	1.358	1.281	1.239	1.099	1.220	1.308	1.021
	Lu_2O_3	< 0.013	< 0.013	< 0.013	< 0.013	< 0.013	< 0.013	< 0.013	< 0.013	< 0.013	< 0.013
	Y_2O_3	6.06	6.17	7.70	7.71	7.33	7.06	7.82	7.79	7.41	6.63
	ThO_2	1.391	1.385	1.704	1.594	1.220	1.168	1.635	1.665	1.608	1.274
	UO_2	0.373	0.412	0.870	0.723	0.490	0.450	0.736	0.741	0.644	0.355
	PbO	0.736	0.759	1.375	1.187	0.823	0.763	1.222	1.243	1.109	0.661
	HfO_2	0.764	0.744	0.631	0.673	0.822	0.792	0.572	0.608	0.720	0.760
	Sc_2O_3	0.022	0.024	0.028	0.023	0.026	0.025	0.027	0.024	0.027	0.020
	Ta_2O_5	0.120	0.140	0.123	0.113	0.208	0.129	< 0.017	< 0.017	0.102	0.131
	Nb_2O_5	2.86	2.83	2.57	2.51	2.35	2.35	2.59	2.59	2.62	2.39
	Total	98.95	99.05	99.17	99.02	99.23	100.25	99.45	98.79	99.67	100.52
Cations per 7 oxygen											
A	Fe	0.3854	0.3933	0.4276	0.4258	0.4041	0.3886	0.4102	0.4184	0.4225	0.3858
	Mn	0.0051	0.0051	0.0057	0.0058	0.0052	0.0056	0.0056	0.0055	0.0056	0.0049
	Mg	0.0089	0.0124	0.0131	0.0139	0.0154	0.0152	0.0019	0.0044	0.0141	0.0098
	Ca	0.4520	0.4386	0.3474	0.3641	0.4024	0.4024	0.3656	0.3617	0.3782	0.4182
	Sum	0.8515	0.8494	0.7938	0.8097	0.8272	0.8118	0.7832	0.7900	0.8203	0.8187
B	Y	0.2119	0.2161	0.2730	0.2741	0.2569	0.2421	0.2744	0.2769	0.2615	0.2277
	Sc	0.0013	0.0014	0.0016	0.0013	0.0015	0.0014	0.0015	0.0014	0.0016	0.0011
	La	0.0070	0.0071	0.0031	0.0031	0.0038	0.0040	0.0032	0.0033	0.0036	0.0046
	Ce	0.0460	0.0457	0.0245	0.0255	0.0285	0.0292	0.0256	0.0256	0.0272	0.0336
	Pr	0.0083	0.0084	0.0055	0.0062	0.0061	0.0061	0.0055	0.0056	0.0059	0.0068
	Nd	0.0374	0.0376	0.0312	0.0322	0.0333	0.0324	0.0316	0.0315	0.0335	0.0357
	Sm	0.0122	0.0125	0.0153	0.0158	0.0138	0.0137	0.0143	0.0148	0.0152	0.0141
	Eu	-	-	-	-	-	-	-	-	-	-
	Gd	0.0182	0.0182	0.0283	0.0275	0.0250	0.0238	0.0270	0.0269	0.0259	0.0225
	Tb	0.0030	0.0032	0.0050	0.0048	0.0044	0.0037	0.0043	0.0046	0.0044	0.0037
	Dy	0.0194	0.0200	0.0351	0.0336	0.0287	0.0273	0.0314	0.0322	0.0301	0.0239
	Ho	0.0037	0.0045	0.0076	0.0067	0.0056	0.0051	0.0060	0.0062	0.0061	0.0043
	Er	0.0150	0.0156	0.0245	0.0238	0.0205	0.0193	0.0217	0.0223	0.0211	0.0161
	Tm	0.0039	0.0041	0.0059	0.0056	0.0048	0.0046	0.0049	0.0050	0.0051	0.0040
	Yb	0.0202	0.0207	0.0272	0.0277	0.0257	0.0244	0.0221	0.0249	0.0265	0.0201
	Lu	–	–	–	–	–	–	–	–	–	–
	Sum	0.4074	0.4151	0.4879	0.4878	0.4585	0.4371	0.4734	0.4811	0.4677	0.4182
C	Zr	1.0593	1.0624	0.9965	1.0149	1.0304	1.0256	1.0279	1.0346	1.0419	1.0778
	Hf	0.0143	0.0140	0.0120	0.0128	0.0155	0.0146	0.0108	0.0116	0.0136	0.0140
	Th	0.0208	0.0208	0.0258	0.0242	0.0183	0.0171	0.0245	0.0253	0.0243	0.0187
	U	0.0055	0.0060	0.0129	0.0108	0.0072	0.0065	0.0108	0.0110	0.0095	0.0051
	Pb	0.0130	0.0134	0.0247	0.0214	0.0146	0.0132	0.0217	0.0224	0.0198	0.0115
	Sum	1.1129	1.1167	1.0719	1.0841	1.0859	1.0771	1.0958	1.1049	1.1091	1.1271
D	Si	0.0239	0.0250	0.0906	0.0387	0.0420	0.0910	0.0780	0.0538	0.0224	0.0517
	Ti	1.5148	1.5046	1.4747	1.5070	1.5072	1.4773	1.4745	1.4834	1.5043	1.4912
	Al	0.0177	0.0196	0.0154	0.0155	0.0279	0.0501	0.0265	0.0204	0.0157	0.0289
	Cr	0.0004	0.0004	0.0005	0.0005	0.0004	0.0003	0.0002	–	–	0.0003
	Ta	0.0022	0.0025	0.0022	0.0021	0.0037	0.0023	–	–	0.0018	0.0023
	Nb	0.0851	0.0844	0.0775	0.0759	0.0699	0.0685	0.0771	0.0783	0.0784	0.0698
	D	1.6441	1.6364	1.6609	1.6396	1.6511	1.6895	1.6563	1.6360	1.6226	1.6441

Table 2 (continued)

		#11	#12	#13	#14	#15	#16	#17	#18	#19	#20
M_I	A	0.8515	0.8494	0.7938	0.8097	0.8272	0.8118	0.7832	0.7900	0.8203	0.8187
	B	0.1485	0.1506	0.2062	0.1903	0.1728	0.1882	0.2168	0.2100	0.1797	0.1813
	Sum	1.0000	1.0000	1.0000	1.0000	1.0000	1.0000	1.0000	1.0000	1.0000	1.0000
M_{II}	C	0.7411	0.7355	0.7183	0.7025	0.7143	0.7511	0.7434	0.7289	0.7120	0.7631
	B	0.2589	0.2645	0.2817	0.2975	0.2857	0.2490	0.2566	0.2711	0.2880	0.2369
	Sum	1.0000	1.0000	1.0000	1.0000	1.0000	1.0000	1.0000	1.0000	1.0000	1.0000
M_{III}	D	1.6441	1.6364	1.6609	1.6396	1.6511	1.6895	1.6563	1.6360	1.6226	1.6441
	Zr	0.3718	0.3812	0.3536	0.3815	0.3716	0.3260	0.3523	0.3760	0.3971	0.3640
	Sum	2.0160	2.0176	2.0145	2.0211	2.0227	2.0155	2.0087	2.0120	2.0198	2.0080
	$M_I + M_{II} + M_{III}$	4.0264	4.0176	4.0145	4.0211	4.0227	4.0155	4.0087	4.0120	4.0198	4.0080

Si content in zirconolites is likely due to secondary fluorescence from adjacent silica and K-feldspar. Sum of cations in each crystallographic site follows the methodology of Wark et al. (1974)

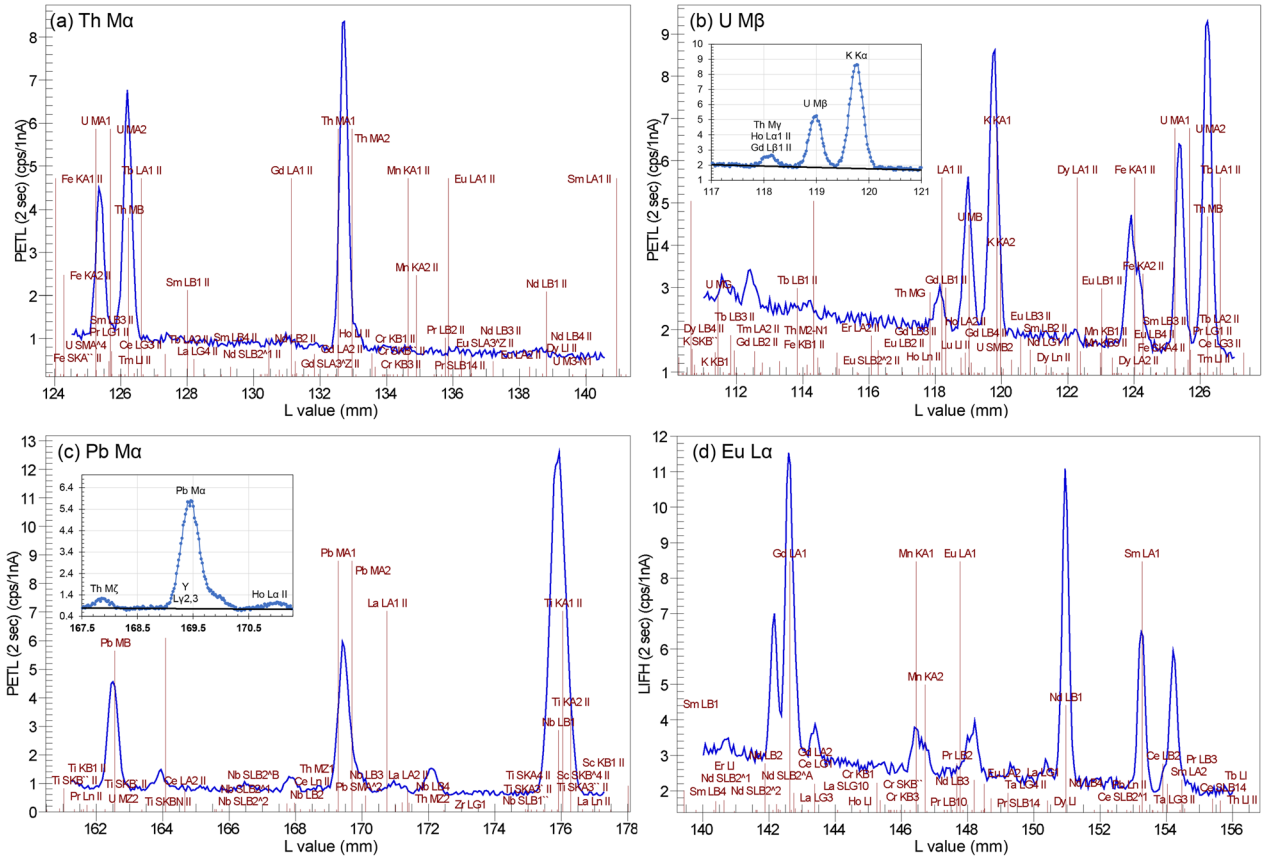

Fig. 2 Wavelength scan simulation performed by PfE around Th Mα (**a**), U Mβ (**b**), Pb Mα (**c**), and Eu Lα (**d**) peaks. The L value (mm) used in the JEOL electron microprobe is the length of the refracted X-ray from the sample to the analyzing crystal. A representative chemical composition of lunar zirconolite measured in this study was used for the simulation under the same analytical condition for quantitative analyses. Interference correction was applied based on the simulation results. No significant interferences were observed for Th Mα (**a**). More detailed wavescan simulations were performed for U Mβ and Pb Mα (insets of b and c). Secondary fluorescence of K Kα from the adjacent K-feldspar is expected to increase K concentrations to ~ 0.25 wt % in zirconolite (Fig. S3), which may interfere with U Mβ (**b**). The interference of Y Lγ2,3 is unavoidable (**c**). Note that the wavescan simulation data are likely to be different from the actual wavescan on the sample and the interferences of Th and K on U and Y on Pb should be corrected with appropriate correction factors. After correction of Nd, Pr, and Mn interferences on the Eu Lα peak, the Eu concentrations became below the detection limit

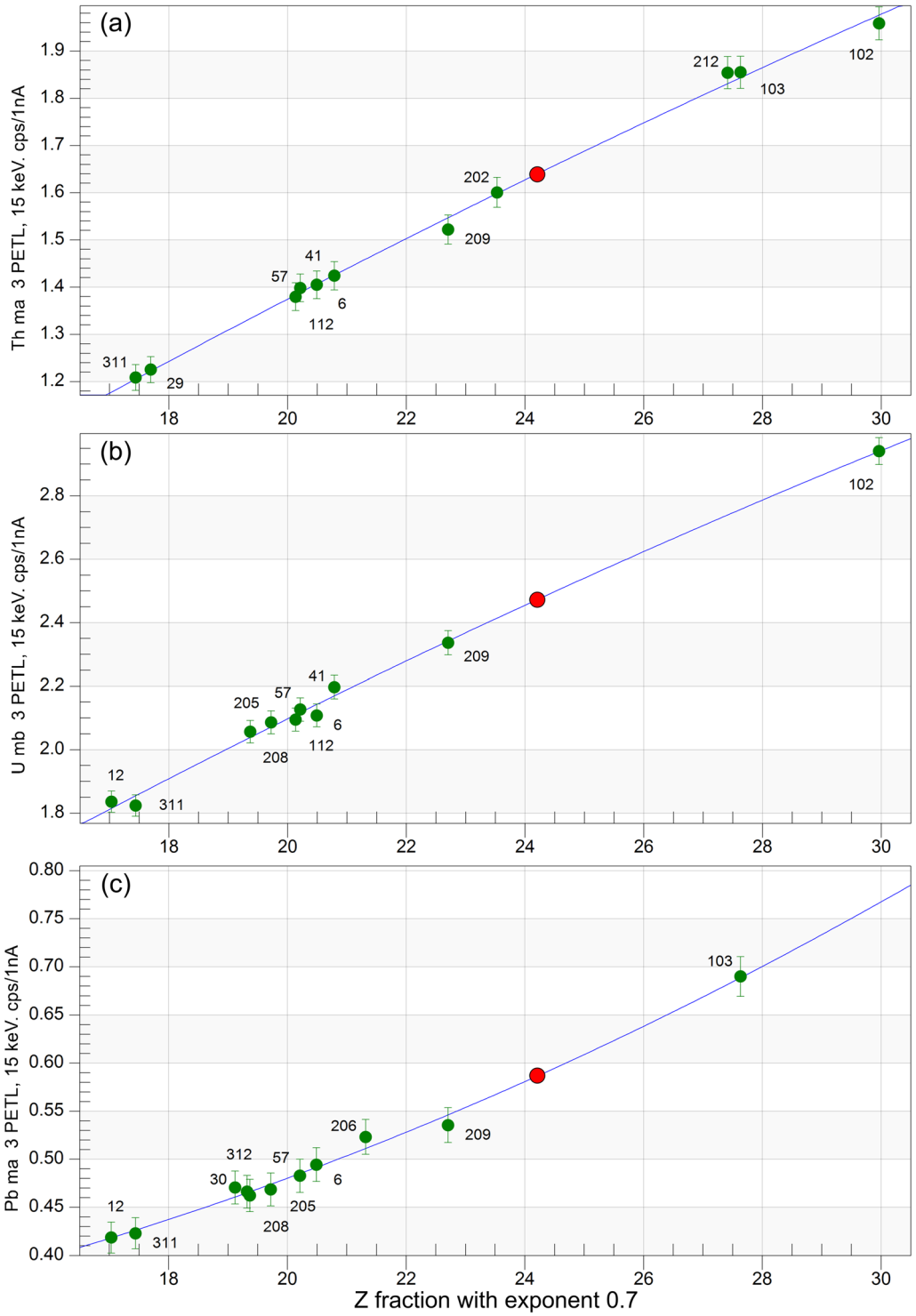

Fig. 3 MAN background curves for Th (**a**), U (**b**), and Pb (**c**). Background intensities were measured at the Th Mα, U Mβ, and Pb Mα peak positions using a 15 keV electron beam with PETL crystal (channel 3) for natural mineral and synthetic compound standards (green circles; listed in Additional file 4: Table S1) that do not contain Th, U, or Pb, respectively. The data were corrected for continuum absorption and a Z fraction average Z was applied using an exponent of 0.7. A 2nd order polynomial was used to best fit the data. The red circle represents the zirconolite. Further details are described in the main text

Interference correction

PfE provides a WDS simulation mode that can produce wavelength scan data of any material of known composition. We used the WDS simulation mode to obtain wavelength scan data near the on-peak wavelengths of the 31 elements analyzed in this study, to find possible peak interferences. For the wavelength simulation of zirconolite, an accelerating voltage of 15 keV and 100 nA beam current and 1 s per step were set. An arbitrary chemical composition of zirconolite from the literature data was used for the first simulation, which allowed us to set potential peak interferences for sample analysis. The wavelength scan simulation using the representative chemical composition of zirconolite in the clast C3 of the DEW 12007 was then used to carefully examine the peak interferences applied to interference corrections. The simulated wavelength scans for Th, U, Pb, and Eu are shown in Fig. 3 and the peak interferences are listed in Table 1.

It should be noted that the actual wavescan data for the elements analyzed in this study will differ from those of the simulation. The most problematic aspect of the simulation is the changing shape of the peaks depending on the analytical conditions and the sample, which can greatly affect the interference correction. Particularly for U and Pb, previous studies for monazite and xenotime discuss the interferences of Th Mγ and K Kα on U Mβ, and Th Mζ and Y Lγ on Pb Mα (e.g., Allaz et al. 2020; Jercinovic and Williams 2005; Suzuki and Kato 2008). Since we did not obtain an actual wavescan data from the zirconolite in this study, we applied the interference correction factors of 0.008 for Th on U and 0.00021 for Th on Pb from Jercinovic and Williams (2005) and 0.0096 for Y on Pb from the YPO_4 standard in this study.

Results and discussion

The chemical compositions of the zirconolites for 31 elements analyzed by electron microprobe using the conditions in Table 1 are listed in Table 2. The concentrations of the analyzed elements are generally above the detection limits, except for Eu and Lu. The cations per 7 oxygen atoms are calculated and assigned using the structural formula, $(M_I)^{2+}(M_{II})^{4+}(M_{III})^{4+}{}_2O_7$, according to the methods described by Wark et al. (1973) (Table 2). It should be noted that the M-line X-rays of Yb, Lu, Hf, and Ta were analyzed in this study (Table 1), but it is not the best choice for the zirconolite analysis due to mutual REE interferences. The L-line X-rays of the elements are recommended like as for monazite and xenotime (Allaz et al. 2020). The results of this study (Table 2) are acceptable because the REE contents of the zirconolite are not high as those of monazite and the appropriate interference corrections for these elements are applied. For the future study, we suggest a recommended analytical setting for the zirconolite analysis by electron microprobe (Additional file 4: Table S3).

SiO_2 contents in zirconolites are generally less than 0.5 wt% (minimum 0.314 wt%) but some of them are above ~ 1.5 wt%. Such high SiO_2 contents are unlikely in the zirconolite lattice structure (Seddio et al. 2013; Wark et al. 1973), so the values may result from the secondary fluorescence of Si from the surrounding high-Si phases. It is well known that the secondary fluorescence effects from neighboring phases can significantly influence the concentrations of trace elements in the analyzed phase (e.g., Llovet et al. 2012). Zirconolites in the C3 clast appear as thin strings with a diameter of 2–3 μm and are surrounded by very high Si-bearing phases, silica and K-feldspar. Thus, the Si X-ray signals in the zirconolite can be strongly affected by silica and K-feldspar. To assess the effects, we simulated for secondary fluorescence effect of Si from the surrounding silica and K-feldspar using CalcZAF software (https://probesoftware.com/download/CalcZAF.msi). The software provides a program called PENFLOUR/FANAL which implements the computer code FANAL to correct for secondary fluorescence (Llovet et al. 2012) and the Monte Carlo simulation program PENEPMA (Llovet and Salvat 2017). Two separate simulations were performed for the zirconolite-silica and the zirconolite-K-feldspar, respectively. The Si concentrations on zirconolite were calculated using secondary fluorescence from the boundary phase (silica and K-feldspar). The concentrations were then summed, assuming that the effects were from both sides of the 3 μm diameter zirconolite (Additional file 3: Fig. S3). The simulation results clearly show that at least ~ 0.3 wt% Si in zirconolites is due to secondary fluorescence effects from adjacent silica and K-feldspar. Thus, we infer that the zirconolites in the granophyric clast C3 in this study have almost no Si, which is consistent with the interpretation of the previous study (Seddio et al. 2013).

In addition, K can be fluoresced from the adjacent K-feldspar although the zirconolite has nominally no K, which Kα interferes U Mβ (Jercinovic and Williams 2005). The simulated secondary fluorescence effect of K is about ~ 0.25 wt% in zirconolite (Additional file 3: Fig. S3). Since K was not measured in the zirconolite, we assumed the interference percentages of K on U for the recalculation of the U concentrations (Table 3), which we will discuss later.

REE patterns normalized to CI chondrite (Palme et al. 2014) are shown in Fig. 4. The overall REE pattern is HREE-rich, with a positive slope for LREEs and a flat to slightly increasing slope for HREEs. The REE pattern in this study is similar to that of lunar granite zirconolites (Seddio et al. 2013), but different from

Table 3 Blank-corrected U, Th, and Pb concentrations from 20 analyses and their recalculated values and ages with different percentages of interference on Pb Mα and U Mβ

Blank-corrected with 91500 zircon								6.8[a]	2.5[b]		7.5[b]		12.5[b]	
U (ppm)	2σ	Th (ppm)	2σ	Pb (ppm)	2σ	Age (Ma)	2σ	Pb (ppm)	U (ppm)	Age (Ma)	U (ppm)	Age (Ma)	U (ppm)	Age (Ma)
5199	50	13,463	75	9628	71	4372	58	9081	5072	4282	4836	4353	4621	4420
3754	48	14,495	77	7999	68	4375	71	7618	3663	4298	3492	4363	3337	4424
3652	47	12,472	73	7053	66	4259	73	6717	3563	4183	3397	4250	3246	4313
3864	48	13,896	76	7921	68	4350	70	7544	3770	4274	3594	4340	3435	4403
3628	48	12,390	74	7029	66	4266	73	6694	3539	4190	3375	4257	3225	4320
3702	47	11,377	72	7125	66	4335	74	6785	3612	4263	3444	4331	3291	4396
5210	50	13,820	76	9647	72	4356	58	9188	5083	4287	4846	4357	4631	4424
5721	50	14,313	77	10,496	73	4374	54	9997	5582	4306	5322	4377	5086	4445
3265	46	11,757	72	6748	65	4367	79	6427	3185	4291	3037	4357	2902	4420
3413	47	12,069	73	6931	65	4343	77	6601	3330	4267	3175	4333	3034	4396
3285	47	12,223	73	6830	65	4352	79	6505	3205	4275	3056	4341	2920	4403
3630	47	12,174	73	7043	66	4284	73	6708	3541	4209	3377	4276	3227	4340
7668	53	14,978	78	12,765	78	4311	45	12,157	7481	4247	7133	4321	6816	4391
6377	51	14,004	76	11,023	74	4326	51	10,498	6221	4260	5932	4333	5668	4402
4321	48	10,720	71	7638	67	4299	67	7274	4215	4231	4019	4302	3841	4370
3963	48	10,265	70	7083	66	4295	72	6746	3867	4226	3687	4296	3523	4363
6491	51	14,370	77	11,347	75	4345	50	10,807	6333	4279	6038	4352	5770	4421
6530	51	14,629	77	11,541	75	4361	50	10,991	6370	4295	6074	4368	5804	4436
5676	50	14,135	76	10,296	73	4353	54	9806	5537	4285	5280	4356	5045	4423
3132	47	11,169	72	6133	64	4251	82	5841	3056	4176	2914	4242	2784	4305
				Weighted mean		4333	14			4262		4332		4398

[a] Interference percentage on Pb. The uncorrected value is greater than the actual (corrected) value by the percentage shown. The total interference % on Pb in zirconolite is dominated by the interference of Y Mγ2,3 on Pb Mα (~6.8%). The interference of Th Mζ on Pb Mα is very small (~0.03%) with the correction factor estimated as a function of Th content (Jercinovic and Williams 2005)

[b] Estimated interference percentages on U. The interference percentage of Th on U is estimated to be ~2.5% using the correction factor of 0.008 for Th (Jercinovic and Williams 2005). Since the K content influenced by K-feldspar was not measured in this study, the K interference percentages of 0, 5, and 10 on Pb are considered, in addition to the ~2.5% interference of Th on U

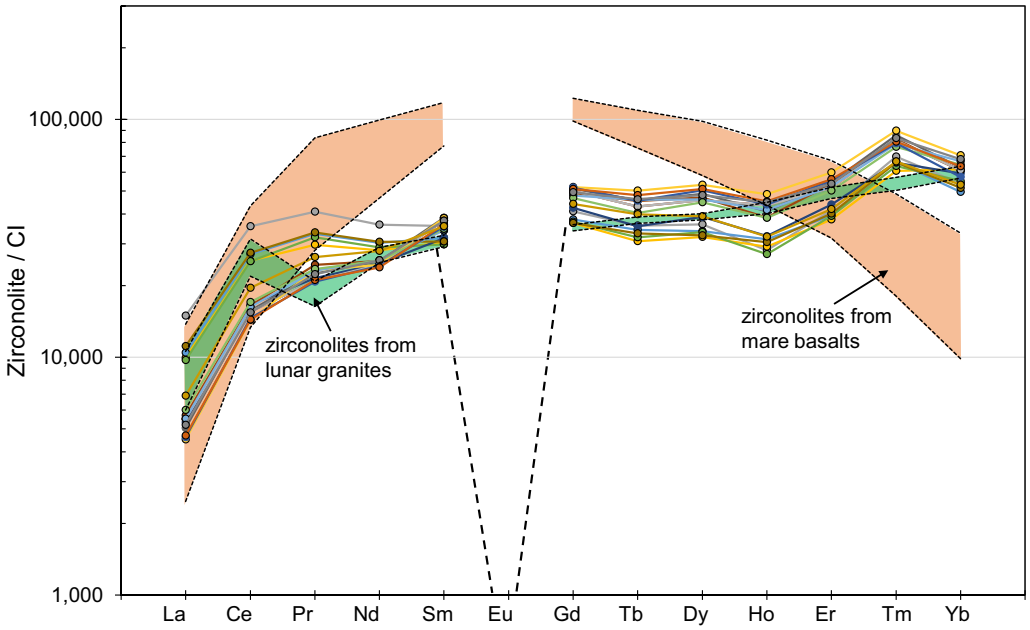

Fig. 4 CI-normalized REE plot of zirconolites in the granophyric clast from the lunar meteorite DEW 12007. The Eu content is below the detection limit after the interference correction. The REE pattern of the zirconolite, characterized by HREE-rich and flat HREE in this study, is similar to that of lunar granite zirconolite (Seddio et al. 2013) but different from a concave shape of the mare basalt zirconolite (Rasmussen et al. 2008). The Eu depletion in the zirconolite explains its late crystallization after plagioclase

that of mare basalt zirconolites, which shows a concave shape with peaks at Sm and Gd (Rasmussen et al. 2008) (Fig. 4). In addition, concentrations of Nd, Sm, Gd, and Tb in basalt zirconolites are up to ~ 2 times higher than those in granite zirconolites (Fig. 4). Eu in the zirconolites was below the detection limit (46 ppm) after peak interference correction (Fig. 3d), resulting in the Eu negative anomaly in the REE pattern (Fig. 4). According to the previous study (Seddio et al. 2013), REE-rich minerals such as merrillite occurred with zirconolite in the lunar granite clast show a complementary REE pattern with zirconolite. If the REE-rich minerals in the C3 clast (Fig. 1) also exhibit a complementary REE pattern, and the Eu negative anomaly in Fig. 4 is a result of early plagioclase crystallization, then the zirconolite in the C3 clast is a late-stage crystallization phase. This is consistent with the occurrence of zirconolite in the C3 clast. Zirconolites are generally fine-grained and occur as elongate strings near tranquillityite and apatite (Figs. 1c–e). Instead, Rasmussen et al. (2008) reported that zirconolite in the mare basalt was formed by decomposition of tranquillityite, which is supported by the decomposition texture of tranquillityite into zirconolite, baddeleyite, ilmenite, and fayalite. However, no previous study has reported such a decomposition texture in lunar granite, and our observations of zirconolite occurrences in granophyric clast C3 are inconsistent with such an interpretation.

Based on the chemical compositions, including REEs, and observations of zirconolites, we conclude that zirconolite was formed by late-stage crystallization, and thus the electron microprobe age of zirconolites in the lunar granitic clast is likely indicative of the crystallization age of the granite.

UO_2, ThO_2, and PbO in the zirconolites are 0.355–0.870, 1.168–1.704, and 0.661–1.375 wt%, respectively. Their elemental wt% (ppm) and uncertainties from counting statistics are listed in Table 3 and are used to date the zirconolites. Electron microprobe ages of the zirconolites were calculated using the equation proposed by (Montel et al. 1996).

$$Pb = \frac{Th}{232}\left(e^{\lambda_{232}t} - 1\right) \times 208 + \frac{U}{238.04}\left(e^{\lambda_{238}t} - 1\right) \times 206 \times 0.9928 + \frac{U}{238.04}\left(e^{\lambda_{235}t} - 1\right) \times 207 \times 0.0072$$

where Pb, U, Th are in ppm, and λ_{232}, λ_{238}, λ_{235} are the radioactive decay constants (4.9475×10^{-11} yr^{-1}, 1.55125×10^{-10} yr^{-1}, and 9.8485×10^{-10} yr^{-1}) of ^{232}Th, ^{238}U, and ^{235}U, respectively (Steiger and Jäger 1977).

Chemical dating assumes that there is almost no initial Pb, so all Pb is radiogenic. A previous study reported U–Pb isotope age of zircon grains in the clast C3 (Fig. 1a), and measured common Pb in the surrounding K-feldspar

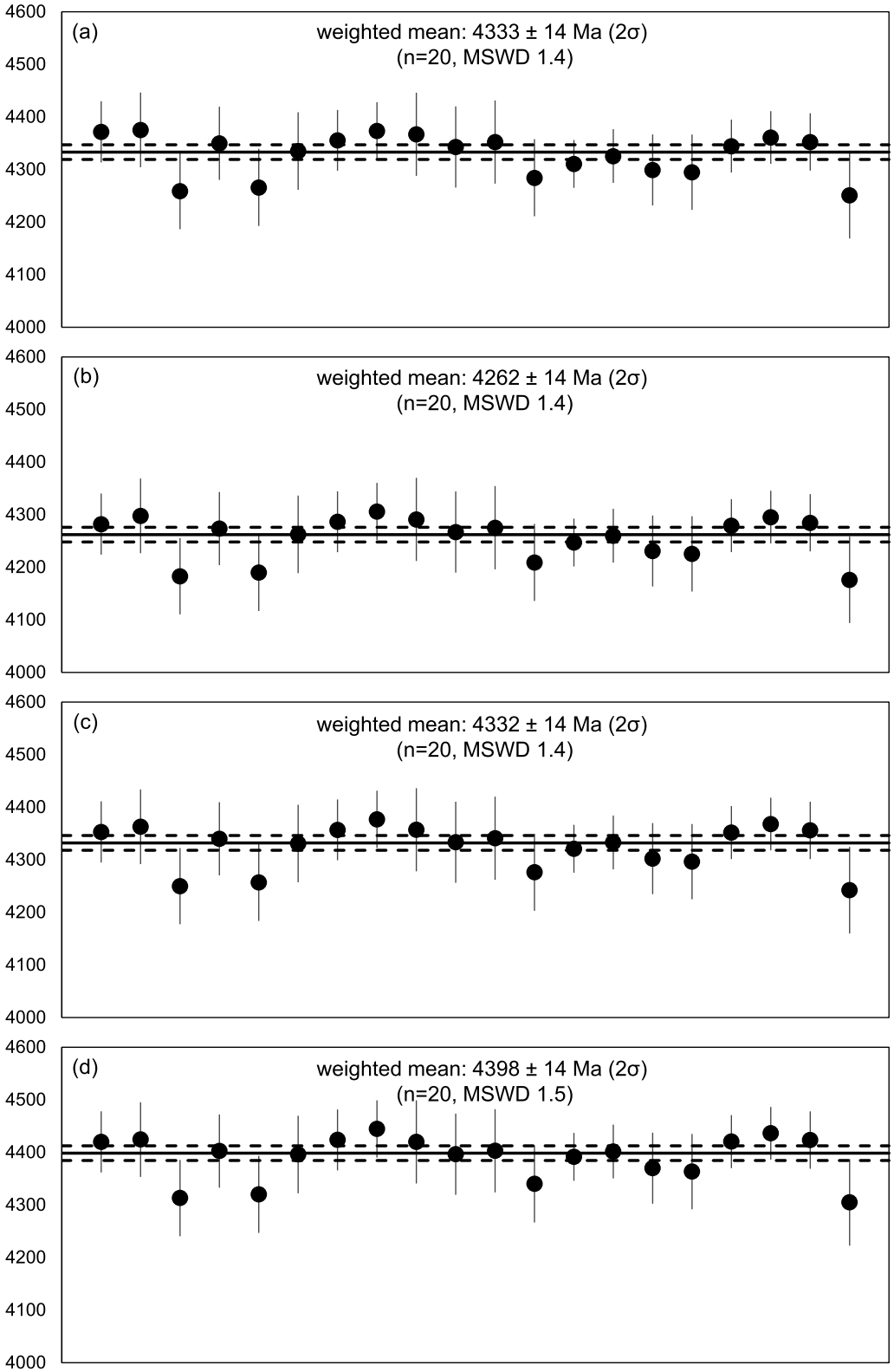

Fig. 5 Electron microprobe ages of the zirconolites in the granitic clast C3 from the lunar meteorite DEW 12007. The ages calculated from the U, Th, and Pb concentrations after the blank correction with the 91500 zircon standard (**a**). The ages after the corrections for the interference percentage of ~ 6.8% on Pb plus interferences of 2.5% (**b**), 7.5% (**c**), and 12.5% on U (**d**), respectively. See discussion in the main text

(Han 2016). The initial ^{206}Pb is determined to be less than 0.05% out of the total ^{206}Pb. Therefore, the above assumption is sound in this study.

The blank-corrected U, Th, and Pb concentrations with the 91500 zircon standard and their recalculated concentration and ages after the interfere corrections are listed in Table 3 and shown in Fig. 5. To correct interferences on U and Pb, we applied the interference correction factors of 0.008 and 0.00021 for Th on U and Pb, respectively, from Jercinovic and Williams (2005). Because Th contents in the zirconolite is less than 1.5 wt%, the interference of Th on U Mβ is mainly by Th M3-N4 (~2.5% in U) and that of Th Mγ on Pb Mα is negligible (<0.03% in Pb) (Jercinovic and Williams 2005). The correction factor for Y on Pb is calculated to be 0.0096 from the YPO_4 standard in this study. Since K was not measured in this study, the interference percentages (0, 5, and 10%) of K on U are assumed. Estimating from the peak interference of K Kα on U Mβ presented in Jercinovic and Williams (2005), the interference percentage of K on the U content would not excess 5% in the zirconolite of this study. If we choose 5% for the interference percentage of K on U with the corrections for the interferences on U and Pb, the weighted mean age is 4332 ± 14 Ma (2σ). The ages without the blank correction followed by the interference corrections are listed in the Additional file 4: Table S2. The weighted mean age is 4327 ± 14 Ma (2σ), if applying 5% interference of K on U. With or without blank correction for U, Th, and Pb in this study, the electron microprobe age of the zirconolites is not significantly changed. This may be due to the sufficiently high concentrations of U, Th, and Pb relative to the detection limits and/or the different matrix of the 91500 zircon standard and zirconolite.

The electron microprobe age of zirconolite in the C3 clast in this study is comparable to the U–Pb age of zircon grains in the same clast obtained by ion microprobe (4340.9 ± 7.5 Ma (2σ); Han (2016)), within uncertainties. The ion microprobe data from zircon grains are slightly discordant in the Terra-Wasserburg diagram (Han 2016), which may imply that there was a chance of Pb loss by a shock event on the Moon. If there was a Pb loss in the zirconolite grains during the shock event, the age determined in this study may infer the lower limit of the crystallization age of the granitic clast C3. Thus, the granophyric clast C3 is one of the oldest granitic rocks from the Moon (Meyer et al. 1996; Nemchin et al. 2008).

Conclusion

Recent advances in trace element analysis by electron microprobe, including MAN background, peak interference, and blank corrections, were applied to this study and enabled us to obtain high-precision chemical composition data of lunar zirconolites from the granitic clast C3. The weighted mean age of the zirconolites after correction for interferences on U and Pb followed by the blank correction with the 91500 zircon is 4332 ± 14 Ma (2σ, $n = 20$), which is in an agreement with the U–Pb age (4340.9 ± 7.5 Ma; 2σ) of zircon grains from the same clast determined by ion microprobe. The precision and accuracy achieved in this study is significantly improved over previously reported electron microprobe ages of lunar zirconolites. However, the lack of interference correction with actual wavescan data is a limitation of this study. We emphasize that the detailed wavescan especially on the U and Pb for the sample studied is essential to figure out any potential interferences and correct them. Because zirconolite is highly resistant to the electron beam, the precision can be further improved by using a longer measurement time and/or higher beam current. Therefore, chemical dating with the electron microprobe can be applied to micrometer-scale U-Th-Pb bearing minerals in extraterrestrial materials, especially for returned samples from the Moon and Mars.

Supplementary Information

The online version contains supplementary material available at https://doi.org/10.1186/s40543-024-00431-7.

Additional file 1 Fig. S1 Monte Carlo simulation of the X-ray generation volume in zirconolite at 15 keV accelerating voltage.

Additional file 2 Fig. S2 Secondary electron (SE) image of a zirconolite after analysis. The apparent pits are probably due to electron beam-induced hydrocarbon deposition. Since there is no charging effect in the SE image, the carbon film was not burned out during the analysis. The apparent pits are larger than the applied beam sizes (spot beam or a 1 μm circular beam) because a 100 nA current beam was not perfectly focused.

Additional file 3 Fig. S3 Secondary fluorescence simulation results. The secondary fluorescence effects for Si and K concentrations in the zirconolite from the boundary to the interior (**a**). Si and K concentration in zirconolite by the secondary fluorescence effects from both silica and K-feldspar (**b**), assuming that the zirconolite is a plate of 3 μm diameter completely surrounded by silica and K-feldspar. The apparent concentrations of Si and K in (**b**) are the sum of the fluorescent Si and K in (**a**) when the zirconolite plate is influenced by the adjacent silica and K-feldspar on both sides.

Additional file 4. Tables S1. Standards used for MAN curve fitting in this study. **Table S2.** U, Th, and Pb concentrations from 20 analyses and their recalculated values and ages with different percentages of interference on Pb Mα and U Mβ. **Table S3.** Recommended analytical setting for zirconolite by electron microprobe.

Acknowledgements

Thorough reviews by an anonymous reviewer and Dr. Julien Allaz were most helpful in preparing the final manuscript, and are greatly appreciated.

Author contributions

CP and HK designed this study and analyzed sample with electron microprobe. CP wrote the draft of the manuscript. CP and HK revised the manuscript critically. All authors read and approved the final version of the manuscript.

Funding
This work was supported by KOPRI grant funded by the Ministry of Oceans and Fisheries (PE24050).

Availability of data and materials
All data generated or analyzed during this study are included in this published article [and its additional files].

Declarations

Competing interest
The authors declare that they have no competing interests.

Received: 5 November 2023 Accepted: 22 March 2024
Published online: 29 March 2024

References

Allaz JM, Williams ML, Jercinovic MJ, Goemann K, Donovan J. Multipoint background analysis: gaining precision and accuracy in microprobe trace element analysis. Microsc Microanal. 2019. https://doi.org/10.1017/s1431927618015660.

Allaz JM, Jercinovic MJ, Williams ML. U-Th-Pb_{TOTAL} dating of REE-phosphate by electron microprobe: review and progress. IOP Conf Ser Mater Sci Eng. 2020. https://doi.org/10.1088/1757-899X/891/1/012001.

Collareta A, D'Orazio M, Gemelli M, Pack A, Folco L. High crustal diversity preserved in the lunar meteorite Mount DeWitt 12007 (Victoria Land, Antarctica). Meteorit Planet Sci. 2016. https://doi.org/10.1111/maps.12597.

Donovan JJ, Pingitore NE. Compositional averaging of continuum intensities in multielement compounds. Microsc Microanal. 2002. https://doi.org/10.1017/S1431927602020160.

Donovan JJ, Tingle TN. An improved mean atomic number background correction for quantitative microanalysis. Microsc Microanal. 1996. https://doi.org/10.1017/S1431927696210013.

Donovan JJ, Lowers HA, Rusk BG. Improved electron probe microanalysis of trace elements in quartz. Am Miner. 2011. https://doi.org/10.2138/am.2011.3631.

Donovan JJ, Singer JW, Armstrong JT. A new EPMA method for fast trace element analysis in simple matrices. Am Miner. 2016. https://doi.org/10.2138/am-2016-5628.

Donovan J, Ducharme A, Schwab JJ, Moy A, Gainsforth Z, Wade B, McMorran B. An improved average atomic number calculation for estimating backscatter and continuum production in compounds. Microsc Microanal. 2023. https://doi.org/10.1093/micmic/ozad069.

Drouin D, Couture AR, Joly D, Tastet X, Aimez V. and Gauvin R. CASINO V2.42—A fast and easy-to-use modeling tool for scanning electron microscopy and microanalysis users. Scanning 2007. https://doi.org/10.1002/sca.20000

Han J, Petrography, geochemistry, and age of granophyre clast in the lunar meteorite DEW 12007, Yonsei University, 2016.

Jercinovic MJ, Williams ML. Analytical perils (and progress) in electron microprobe trace element analysis applied to geochronology: background acquisition, interferences, and beam irradiation effects. Am Miner. 2005. https://doi.org/10.2138/am.2005.1422.

Llovet X, Salvat F. PENEPMA: a Monte Carlo program for the simulation of X-ray emission in electron probe microanalysis. Microsc Microanal. 2017. https://doi.org/10.1017/s1431927617000526.

Llovet X, Pinard PT, Donovan JJ, Salvat F. Secondary fluorescence in electron probe microanalysis of material couples. J Phys D Appl Phys. 2012. https://doi.org/10.1088/0022-3727/45/22/225301.

Luo JS, Sung CS, Hsu WS, Huang LY, Russell JD. Electron beam induced carbon deposition using hydrocarbon contamination for XTEM analysis. Microelectron Reliab. 2010. https://doi.org/10.1016/j.microrel.2010.07.046.

Meyer C, Williams IS, Compston W. Uranium-lead ages for lunar zircons: evidence for a prolonged period of granophyre formation from 4.32 to 3.88 Ga. Meteorit Planet Sci. 1996. https://doi.org/10.1111/j.1945-5100.1996.tb02075.x.

Montel J-M, Foret S, Veschambre M, Nicollet C, Provost A. Electron microprobe dating of monazite. Chem Geol. 1996. https://doi.org/10.1016/0009-2541(96)00024-1.

Montel J-M, Kato T, Enami M, Cocherie A, Finger F, Williams M, Jercinovic M. Electron-microprobe dating of monazite: the story. Chem Geol. 2018. https://doi.org/10.1016/j.chemgeo.2017.11.001.

Moy A, Fournelle J, Nachlas W, Dungan M, Locock A, Bullock E, Donovan J, Cathey H, Allaz J. and Handt AVD, On the importance of including all elements in the EPMA matrix correction. Microscopy and Microanalysis 2023. https://doi.org/10.1093/micmic/ozad067.424

Nemchin AA, Pidgeon RT, Whitehouse MJ, Vaughan JP, Meyer C. SIMS U-Pb study of zircon from Apollo 14 and 17 breccias: implications for the evolution of lunar KREEP. Geochim Cosmochim Acta. 2008. https://doi.org/10.1016/j.gca.2007.11.009.

Norman MD. and Nemchin, A.A. A 4.2 billion year old impact basin on the Moon: U-Pb dating of zirconolite and apatite in lunar melt rock 67955. Earth Planet Sci Lett. 2014. https://doi.org/10.1016/j.epsl.2013.11.040.

Palme H, Lodders K, Jones A. Solar system abundances of the elements. In: Holland HD, Turekian KK, editors. Treatise on geochemistry. Planets, asteriods, comets and the solar system. Oxford: Elsevier; 2014. p. 15–36. https://doi.org/10.1016/B978-0-08-095975-7.00118-2.

Postek MT. An approach to the reduction of hydrocarbon contamination in the scanning electron microscope. Scanning. 1996. https://doi.org/10.1002/sca.1996.4950180402.

Rasmussen B, Fletcher IR. Zirconolite: a new U-Pb chronometer for mafic igneous rocks. Geology. 2004. https://doi.org/10.1130/g20658.1.

Rasmussen B, Fletcher IR, Muhling JR. Pb/Pb geochronology, petrography and chemistry of Zr-rich accessory minerals (zirconolite, tranquillityite and baddeleyite) in mare basalt 10047. Geochim Cosmochim Acta. 2008. https://doi.org/10.1016/j.gca.2008.09.010.

Seddio SM, Jolliff BL, Korotev RL, Zeigler RA. Petrology and geochemistry of lunar granite 12032, 366–19 and implications for lunar granite petrogenesis. Am Miner. 2013. https://doi.org/10.2138/am.2013.4330.

Steiger RH, Jäger E. Subcommission on geochronology: convention on the use of decay constants in geo- and cosmochronology. Earth Planet Sci Lett. 1977. https://doi.org/10.1016/0012-821X(77)90060-7.

Suzuki K, Kato T. CHIME dating of monazite, xenotime, zircon and polycrase: protocol, pitfalls and chemical criterion of possibly discordant age data. Gondwana Res. 2008. https://doi.org/10.1016/j.gr.2008.01.005.

Vladar A, Postek M. Electron beam-induced sample contamination in the SEM. Microsc Microanal. 2005. https://doi.org/10.1017/S1431927605507785.

Wang N, Mao Q, Zhang T, Hao J, Lin Y. NanoSIMS and EPMA dating of lunar zirconolite. Prog Earth Planet Sci. 2021. https://doi.org/10.1186/s40645-021-00446-3.

Wark D, Reid A, Lovering J and El Goresy A Zirconolite (versus zirkelite) in lunar rocks. Lunar Planet. Sci. 1973.

Wiedenbeck M, Hanchar JM, Peck WH, Sylvester P, Valley J, Whitehouse M, Kronz A, Morishita Y, Nasdala L, Fiebig J, Franchi I, Girard J-P, Greenwood RC, Hinton R, Kita N, Mason PRD, Norman M, Ogasawara M, Piccoli PM, Rhede D, Satoh H, Schulz-Dobrick B, Skår O, Spicuzza M, Terada K, Tindle A, Togashi S, Vennemann T, Xie Q, Zheng Y-F. Further characterisation of the 91500 zircon crystal. Geostds Geoan Res. 2004. https://doi.org/10.1111/j.1751-908X.2004.tb01041.x.

Publisher's Note

Springer Nature remains neutral with regard to jurisdictional claims in published maps and institutional affiliations.